Measurement of the electron structure function F2e at LEP energies

Abdallah, J.; et al., [Unknown]; van Vulpen, I.

Link to publication

PHYSICS LETTERS B

Measurement of the electron structure function F_2^e at LEP energies

DELPHI Collaboration

J. Abdallah [ab], P. Abreu [y], W. Adam [be], P. Adzic [m], T. Albrecht [s], R. Alemany-Fernandez [j],
T. Allmendinger [s], P.P. Allport [z], U. Amaldi [af], N. Amapane [ax], S. Amato [bb], E. Anashkin [am],
A. Andreazza [ae], S. Andringa [y], N. Anjos [y], P. Antilogus [ab], W-D. Apel [s], Y. Arnoud [p], S. Ask [j],
B. Asman [aw], J.E. Augustin [ab], A. Augustinus [j], P. Baillon [j], A. Ballestrero [ay], P. Bambade [w],
R. Barbier [ad], D. Bardin [r], G.J. Barker [bg], A. Baroncelli [ap], M. Battaglia [j], M. Baubillier [ab],
K-H. Becks [bh], M. Begalli [h], A. Behrmann [bh], K. Belous [as], E. Ben-Haim [ab], N. Benekos [ai],
A. Benvenuti [f], C. Berat [p], M. Berggren [ab], D. Bertrand [c], M. Besancon [aq], N. Besson [aq],
D. Bloch [k], M. Blom [ah], M. Bluj [bf], M. Bonesini [af], M. Boonekamp [aq], P.S.L. Booth [z,1],
G. Borisov [x], O. Botner [bc], B. Bouquet [w], T.J.V. Bowcock [z], I. Boyko [r], M. Bracko [at],
R. Brenner [bc], E. Brodet [al], P. Bruckman [t], J.M. Brunet [i], B. Buschbeck [be], P. Buschmann [bh],
M. Calvi [af], T. Camporesi [j], V. Canale [ao], F. Carena [j], N. Castro [y], F. Cavallo [f], M. Chapkin [as],
Ph. Charpentier [j], P. Checchia [am], R. Chierici [ad], P. Chliapnikov [as], J. Chudoba [n], S.U. Chung [j],
K. Cieslik [t], P. Collins [j], R. Contri [o], G. Cosme [w], F. Cossutti [az], M.J. Costa [bd], D. Crennell [an],
J. Cuevas [ak], J. D'Hondt [c], T. da Silva [bb], W. Da Silva [ab], G. Della Ricca [az], A. De Angelis [ba],
W. De Boer [s], C. De Clercq [c], B. De Lotto [ba], N. De Maria [ax], A. De Min [am], L. de Paula [bb],
L. Di Ciaccio [ao], A. Di Simone [ao], K. Doroba [bf], J. Drees [bh], G. Eigen [e], T. Ekelof [bc], M. Ellert [bc],
M. Elsing [j], M.C. Espirito Santo [y], G. Fanourakis [m], D. Fassouliotis [m,d], M. Feindt [s],
J. Fernandez [ar], A. Ferrer [bd], F. Ferro [o], U. Flagmeyer [bh], H. Foeth [j], E. Fokitis [ai],
F. Fulda-Quenzer [w], J. Fuster [bd], M. Gandelman [bb], C. Garcia [bd], Ph. Gavillet [j], E. Gazis [ai],
R. Gokieli [bf,1], B. Golob [at,av], G. Gomez-Ceballos [ar], P. Gonçalves [y], E. Graziani [ap],
G. Grosdidier [w], K. Grzelak [bf], J. Guy [an], C. Haag [s], A. Hallgren [bc], K. Hamacher [bh],
K. Hamilton [al], S. Haug [aj], F. Hauler [s], V. Hedberg [ac], M. Hennecke [s], J. Hoffman [bf],
S-O. Holmgren [aw], P.J. Holt [j], M.A. Houlden [z], J.N. Jackson [z], G. Jarlskog [ac], P. Jarry [aq],
D. Jeans [al], E.K. Johansson [aw], P. Jonsson [ad], C. Joram [j], L. Jungermann [s], F. Kapusta [ab],
S. Katsanevas [ad], E. Katsoufis [ai], G. Kernel [at], B.P. Kersevan [at,av], U. Kerzel [s], B.T. King [z],
N.J. Kjaer [j], P. Kluit [ah], P. Kokkinias [m], C. Kourkoumelis [d], O. Kouznetsov [r], Z. Krumstein [r],
M. Kucharczyk [t], J. Lamsa [a], G. Leder [be], F. Ledroit [p], L. Leinonen [aw], R. Leitner [ag],
J. Lemonne [c], V. Lepeltier [w,1], T. Lesiak [t], W. Liebig [bh], D. Liko [be], A. Lipniacka [e], J.H. Lopes [bb],
J.M. Lopez [ak], D. Loukas [m], P. Lutz [aq], L. Lyons [al], J. MacNaughton [be], A. Malek [bh],
S. Maltezos [ai], F. Mandl [be], J. Marco [ar], R. Marco [ar], B. Marechal [bb], M. Margoni [am],
J-C. Marin [j], C. Mariotti [j], A. Markou [m], C. Martinez-Rivero [ar], J. Masik [n],
N. Mastroyiannopoulos [m], F. Matorras [ar], C. Matteuzzi [af], F. Mazzucato [am], M. Mazzucato [am],
R. Mc Nulty [z], C. Meroni [ae], E. Migliore [ax], W. Mitaroff [be], U. Mjoernmark [ac], T. Moa [aw],
M. Moch [s], K. Moenig [l], R. Monge [o], J. Montenegro [ah], D. Moraes [bb], S. Moreno [y],
P. Morettini [o], U. Mueller [bh], K. Muenich [bh], M. Mulders [ah], L. Mundim [h], W. Murray [an],
B. Muryn [u], G. Myatt [al], T. Myklebust [aj], M. Nassiakou [m], F. Navarria [f], K. Nawrocki [bf],
S. Nemecek [n], R. Nicolaidou [aq], M. Nikolenko [r,k], A. Oblakowska-Mucha [u], V. Obraztsov [as],

A. Olshevski [r], A. Onofre [y], R. Orava [q], K. Osterberg [q], A. Ouraou [aq], A. Oyanguren [bd], M. Paganoni [af], S. Paiano [f], J.P. Palacios [z], H. Palka [t,1], Th.D. Papadopoulou [ai], L. Pape [j], C. Parkes [aa], F. Parodi [o], U. Parzefall [j], A. Passeri [ap], O. Passon [bh], L. Peralta [y], V. Perepelitsa [bd], A. Perrotta [f], A. Petrolini [o], J. Piedra [ar], L. Pieri [am], F. Pierre [aq,1], M. Pimenta [y], E. Piotto [j], T. Podobnik [at,av], V. Poireau [j], M.E. Pol [g], G. Polok [t], V. Pozdniakov [r], N. Pukhaeva [r], A. Pullia [af], D. Radojicic [al], P. Rebecchi [j], J. Rehn [s], D. Reid [ah], R. Reinhardt [bh], P. Renton [al], F. Richard [w], J. Ridky [n], M. Rivero [ar], D. Rodriguez [ar], A. Romero [ax], P. Ronchese [am], P. Roudeau [w], T. Rovelli [f], V. Ruhlmann-Kleider [aq], D. Ryabtchikov [as], A. Sadovsky [r], L. Salmi [q], J. Salt [bd], C. Sander [s], A. Savoy-Navarro [ab], U. Schwickerath [j], R. Sekulin [an], M. Siebel [bh], A. Sisakian [r,1], W. Slominski [v], G. Smadja [ad], O. Smirnova [ac], A. Sokolov [as], A. Sopczak [x], R. Sosnowski [bf], T. Spassov [j], M. Stanitzki [s], A. Stocchi [w], J. Strauss [be], B. Stugu [e], M. Szczekowski [bf], M. Szeptycka [bf], T. Szumlak [u], J. Szwed [v], T. Tabarelli [af], F. Tegenfeldt [bc], J. Timmermans [ah], L. Tkatchev [r], M. Tobin [z], S. Todorovova [n], B. Tomé [y], A. Tonazzo [af], P. Tortosa [bd], P. Travnicek [n], D. Treille [j], G. Tristram [i], M. Trochimczuk [bf], C. Troncon [ae], M-L. Turluer [aq], I.A. Tyapkin [r], P. Tyapkin [r], S. Tzamarias [m], V. Uvarov [as], G. Valenti [f], P. Van Dam [ah], J. Van Eldik [j], N. van Remortel [b], I. Van Vulpen [ah], G. Vegni [ae], F. Veloso [y], W. Venus [an], P. Verdier [ad], V. Verzi [ao], D. Vilanova [aq], L. Vitale [az], V. Vrba [n], H. Wahlen [bh], A.J. Washbrook [z], C. Weiser [s], D. Wicke [bh], J. Wickens [c], G. Wilkinson [al], M. Winter [k], M. Witek [t], O. Yushchenko [as], A. Zalewska [t], P. Zalewski [bf], D. Zavrtanik [au], V. Zhuravlov [r], N.I. Zimin [r], A. Zintchenko [r], M. Zupan [m]

[a] *Department of Physics and Astronomy, Iowa State University, Ames, IA 50011-3160, USA*
[b] *Physics Department, Universiteit Antwerpen, Universiteitsplein 1, B-2610 Antwerpen, Belgium*
[c] *IIHE, ULB-VUB, Pleinlaan 2, B-1050 Brussels, Belgium*
[d] *Physics Laboratory, University of Athens, Solonos Str. 104, GR-10680 Athens, Greece*
[e] *Department of Physics, University of Bergen, Allégaten 55, NO-5007 Bergen, Norway*
[f] *Dipartimento di Fisica, Università di Bologna and INFN, Viale C. Berti Pichat 6/2, IT-40127 Bologna, Italy*
[g] *Centro Brasileiro de Pesquisas Físicas, rua Xavier Sigaud 150, BR-22290 Rio de Janeiro, Brazil*
[h] *Inst. de Física, Univ. Estadual do Rio de Janeiro, rua São Francisco Xavier 524, Rio de Janeiro, Brazil*
[i] *Collège de France, Lab. de Physique Corpusculaire, IN2P3-CNRS, FR-75231 Paris Cedex 05, France*
[j] *CERN, CH-1211 Geneva 23, Switzerland*
[k] *Institut Pluridisciplinaire Hubert Curien, Université de Strasbourg, IN2P3-CNRS, BP28, FR-67037 Strasbourg Cedex 2, France*
[l] *DESY-Zeuthen, Platanenallee 6, D-15735 Zeuthen, Germany* [2]
[m] *Institute of Nuclear Physics, N.C.S.R. Demokritos, P.O. Box 60228, GR-15310 Athens, Greece*
[n] *FZU, Inst. of Phys. of the C.A.S. High Energy Physics Division, Na Slovance 2, CZ-182 21, Praha 8, Czech Republic*
[o] *Dipartimento di Fisica, Università di Genova and INFN, Via Dodecaneso 33, IT-16146 Genova, Italy*
[p] *Laboratoire de Physique Subatomique et de Cosmologie, Université Joseph Fourier Grenoble 1, CNRS/IN2P3, Institut Polytechnique de Grenoble, FR-38026 Grenoble Cedex, France*
[q] *Helsinki Institute of Physics and Department of Physics, P.O. Box 64, FIN-00014 University of Helsinki, Finland*
[r] *Joint Institute for Nuclear Research, Dubna, Head Post Office, P.O. Box 79, RU-101 000 Moscow, Russian Federation*
[s] *Institut für Experimentelle Kernphysik, Universität Karlsruhe, Postfach 6980, DE-76128 Karlsruhe, Germany*
[t] *Henryk Niewodniczanski Institute of Nuclear Physics Polish Academy of Sciences, Krakow, Poland*
[u] *AGH – University of Science and Technology, Faculty of Physics and Applied Computer Science, Krakow, Poland*
[v] *Department of Physics, Jagellonian University, Krakow, Poland*
[w] *LAL, Univ Paris-Sud, CNRS/IN2P3, Orsay, France*
[x] *School of Physics and Chemistry, University of Lancaster, Lancaster LA1 4YB, UK*
[y] *LIP, IST, FCUL, Av. Elias Garcia, 14-1°, PT-1000 Lisboa Codex, Portugal*
[z] *Department of Physics, University of Liverpool, P.O. Box 147, Liverpool L69 3BX, UK*
[aa] *Dept. of Physics and Astronomy, Kelvin Building, University of Glasgow, Glasgow G12 8QQ, UK*
[ab] *LPNHE, IN2P3-CNRS, Univ. Paris VI et VII, 4 place Jussieu, FR-75252 Paris Cedex 05, France*
[ac] *Department of Physics, University of Lund, Sölvegatan 14, SE-223 63 Lund, Sweden*
[ad] *Université Claude Bernard de Lyon, IPNL, IN2P3-CNRS, FR-69622 Villeurbanne Cedex, France*
[ae] *Dipartimento di Fisica, Università di Milano and INFN-Milano, Via Celoria 16, IT-20133 Milan, Italy*
[af] *Dipartimento di Fisica, Univ. di Milano-Bicocca and INFN-Milano, Piazza della Scienza 3, IT-20126 Milan, Italy*
[ag] *IPNP of MFF, Charles Univ., Areal MFF, V Holesovickach 2, CZ-180 00, Praha 8, Czech Republic*
[ah] *NIKHEF, Postbus 41882, NL-1009 DB Amsterdam, The Netherlands*
[ai] *National Technical University, Physics Department, Zografou Campus, GR-15773 Athens, Greece*
[aj] *Physics Department, University of Oslo, Blindern, NO-0316 Oslo, Norway*
[ak] *Dpto. Fisica, Univ. Oviedo, Avda. Calvo Sotelo s/n, ES-33007 Oviedo, Spain*
[al] *Department of Physics, University of Oxford, Keble Road, Oxford OX1 3RH, UK*
[am] *Dipartimento di Fisica, Università di Padova and INFN, Via Marzolo 8, IT-35131 Padua, Italy*
[an] *Rutherford Appleton Laboratory, Chilton, Didcot OX11 OQX, UK*
[ao] *Dipartimento di Fisica, Università di Roma II and INFN, Tor Vergata, IT-00173 Rome, Italy*
[ap] *Dipartimento di Fisica, Università di Roma III and INFN, Via della Vasca Navale 84, IT-00146 Rome, Italy*
[aq] *DAPNIA/Service de Physique des Particules, CEA-Saclay, FR-91191 Gif-sur-Yvette Cedex, France*
[ar] *Instituto de Fisica de Cantabria (CSIC-UC), Avda. los Castros s/n, ES-39006 Santander, Spain*
[as] *Institute for High Energy Physics, 142281 Protvino, Moscow region, Russian Federation*

[at] *J. Stefan Institute, Jamova 39, SI-1000 Ljubljana, Slovenia*
[au] *Laboratory for Astroparticle Physics, University of Nova Gorica, Kostanjeviska 16a, SI-5000 Nova Gorica, Slovenia*
[av] *Department of Physics, University of Ljubljana, SI-1000 Ljubljana, Slovenia*
[aw] *Fysikum, Stockholm University, Box 6730, SE-113 85 Stockholm, Sweden*
[ax] *Dipartimento di Fisica Sperimentale, Università di Torino and INFN, Via P. Giuria 1, IT-10125 Turin, Italy*
[ay] *INFN Sezione di Torino and Dipartimento di Fisica Teorica, Università di Torino, Via Giuria 1, IT-10125 Turin, Italy*
[az] *Dipartimento di Fisica, Università di Trieste and INFN, Via A. Valerio 2, IT-34127 Trieste, Italy*
[ba] *Istituto di Fisica, Università di Udine and INFN, IT-33100 Udine, Italy*
[bb] *Univ. Federal do Rio de Janeiro, C.P. 68528 Cidade Univ., Ilha do Fundão, BR-21945-970 Rio de Janeiro, Brazil*
[bc] *Department of Radiation Sciences, University of Uppsala, P.O. Box 535, SE-751 21 Uppsala, Sweden*
[bd] *IFIC, Valencia-CSIC, and D.F.A.M.N., U. de Valencia, Avda. Dr. Moliner 50, ES-46100 Burjassot (Valencia), Spain*
[be] *Institut für Hochenergiephysik, Österr. Akad. d. Wissensch., Nikolsdorfergasse 18, AT-1050 Vienna, Austria*
[bf] *Inst. Nuclear Studies and University of Warsaw, Ul. Hoza 69, PL-00681 Warsaw, Poland*
[bg] *University of Warwick, Coventry CV4 7AL, UK [2]*
[bh] *Fachbereich Physik, University of Wuppertal, Postfach 100 127, DE-42097 Wuppertal, Germany*

A R T I C L E   I N F O

A B S T R A C T

The hadronic part of the electron structure function F_2^e has been measured for the first time, using e^+e^- data collected by the DELPHI experiment at LEP, at centre-of-mass energies of $\sqrt{s} = 91.2$–209.5 GeV. The data analysis is simpler than that of the measurement of the photon structure function. The electron structure function F_2^e data are compared to predictions of phenomenological models based on the photon structure function. It is shown that the contribution of large target photon virtualities is significant. The data presented can serve as a cross-check of the photon structure function F_2^γ analyses and help in refining existing parameterisations.

1. Introduction

The process $e^+e^- \to e^+e^- X$, where X is an arbitrary hadronic final state, can be used to determine both the photon [1–5] and electron [6–10] hadronic structure functions. The photon structure function F_2^γ has been studied both theoretically and experimentally for many years (see [11,12] and references therein).

Experimental results on the electron structure function F_2^e are presented for the first time in this Letter.

Although both analyses start from the same set of events the procedures are quite different mainly due to different kinematics. In the photon case (Fig. 1(a)) the spectrum of virtual photons emitted by the (untagged) electron is strongly peaked at small virtualities P^2 (this quantity can be expressed in terms of the untagged electron four-momenta, $P^2 = -(p - p')^2$). Many analyses therefore use the real photon approximation $P^2 \approx (m_e)^2 \approx 0$. However, higher target photon virtualities play a role [13,14,10]. The problem does not appear in the electron case (Fig. 1(b)), where the photon scatters on a real particle. Another difference is the determination of the Bjorken variables x (z) representing the fraction of the struck parton momentum with respect to the photon (electron) target. In the first case, since the photon momentum is not known, the total hadronic mass W, which cannot be well determined as the majority of hadrons are going into the beam pipe, must be used to determine x,

$$x \approx \frac{Q^2}{Q^2 + W^2 + P^2}, \tag{1}$$

where $Q^2 = -(k - k')^2$ is the negative momentum squared of the deeply virtual (probing) photon. The z variable for the electron is determined directly – as in the classical deep inelastic scattering i.e. from the scattered electron variables only (see below). A certain drawback of the electron structure function F_2^e is its expected
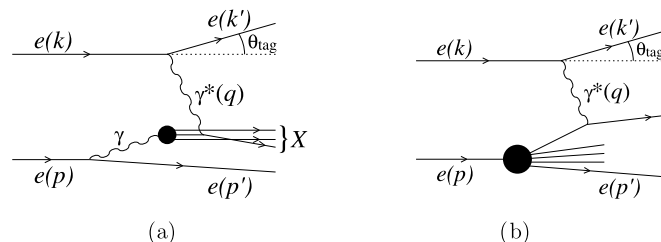

Fig. 1. Deep inelastic scattering (DIS) on a photon target (a), and on an electron target (b); p, p', k and k' denote the corresponding four-momenta and q is the four-momentum of the exchanged photon.

shape, that is dominated by the rapidly changing photon distribution, and is a direct consequence of its formal definition as a convolution of the photon structure function and photon flux (see also discussion in the following text). Hence the data can be reanalysed in terms of the electron structure function F_2^e and the results compared to the usual photon structure function analysis. One can expect that these two complementary electron and photon structure function measurements will help to improve phenomenological parameterisations of the quark and gluon content inside the photon and the electron.

The case of the electron structure function is illustrated in Fig. 1(b). The upper (tagged) electron emits a photon of high virtuality $Q^2 = -q^2$ which scatters off the target electron constituents. The cross-section for such a process under the assumption that $Q^2 \gg P^2$, is:

$$\frac{d^2\sigma(ee \to eeX)}{dz dQ^2} = \frac{2\pi\alpha^2}{zQ^4}\big[(1 + (1-y)^2)F_2^e(z, Q^2) - y^2 F_L^e(z, Q^2)\big], \tag{2}$$

where

$$y = 1 - (E_{\text{tag}}/E)\cos^2(\theta_{\text{tag}}/2), \tag{3}$$

with E, E_{tag} and θ_{tag} being the initial energy, final energy and scattering angle, respectively, of the detected electron or positron

---

[1] Deceased.
[2] Current address.

(called hereafter 'tagged electron') and α is the fine structure constant. The electron structure functions $F_2^e(z, Q^2)$ and $F_L^e(z, Q^2)$ are related to the transverse and longitudinal polarisation states of the probing photon. The parton momentum fraction, z, is defined in the standard (deep inelastic) way:

$$z = \frac{Q^2}{2pq} = \frac{\sin^2(\theta_{tag}/2)}{E/E_{tag} - \cos^2(\theta_{tag}/2)}, \tag{4}$$

and is measured using only the kinematics of the tagged electron. The virtuality of the probing photon can be also expressed in terms of E, E_{tag}, θ_{tag} as follows:

$$Q^2 = 4EE_{tag}\sin^2(\theta_{tag}/2). \tag{5}$$

At leading order, the structure function $F_2^e(z, Q^2)$, which dominates the cross-section at small y, has a simple partonic interpretation:

$$F_2^e(z, Q^2) = z \sum_{i=q,\bar{q}} e_i^2 f_i^e(z, Q^2), \tag{6}$$

where e_i and f_i^e are the i-th quark/anti-quark charge and density.

In e^+e^- experiments the DIS e–γ hadronic cross-section is expressed in terms of two real photon structure functions $F_2^\gamma(x, Q^2)$ and $F_L^\gamma(x, Q^2)$ which leads to a formula analogous to (2)

$$\frac{d^2\sigma(e\gamma \to eX)}{dxdQ^2} = \frac{2\pi\alpha^2}{xQ^4}\Big[\big(1 + (1-y)^2\big)F_2^\gamma(x, Q^2) - y^2 F_L^\gamma(x, Q^2)\Big], \tag{7}$$

where F_2^γ, F_L^γ are the photon structure functions related to the transverse and longitudinal polarisation states of the probing photon respectively.

The differential cross section $\sigma(ee \to eeX)$ is obtained from the corresponding cross section with a photon target, $\sigma(e\gamma \to eX)$, by weighting the latter with the density of photons in the target electron $f_\gamma^e(y_\gamma, P^2)$ (photon flux). The photon flux depends on the target photon virtuality, P^2:

$$f_\gamma^e(y_\gamma, P^2) = \frac{\alpha}{2\pi P^2}\left[\frac{1 + (1-y_\gamma)^2}{y_\gamma} - 2y_\gamma \frac{m_e^2}{P^2}\right], \tag{8}$$

where y_γ is the ratio of the energies of the target photon and the beam, and m_e is the electron mass.

In [6–10] the Q^2 evolution and asymptotic solutions for the electron structure function have been studied. This approach has also been compared with the 'photon structure function' approach. Although the experimental measurements of F_2^e and F_2^γ are quite different the functions have a simple theoretical relation:

$$F_{2/L}^e(z, Q^2, P_{max}^2)$$
$$= \int_z^1 dy_\gamma \int_{P_{min}^2}^{P_{max}^2} dP^2 f_\gamma^e(y_\gamma, P^2) F_{2/L}^\gamma(z/y_\gamma, Q^2, P^2), \tag{9}$$

where $P_{min}^2 = m_e^2 y_\gamma^2/(1-y_\gamma)$ and P_{max}^2 is the maximum value of the target photon virtuality and is fixed by the electron detector (STIC – The Small angle TIle Calorimeter) acceptance (see Section 2.1) and the anti-tag condition.

The P^2 variable is not measurable for single tag events and, as discussed in detail in [9], the extraction of a 'real' photon structure function, F_2^γ, is based on the Weizsäcker–Williams approximation, where P^2 is set to zero in $F_{2/L}^\gamma(x, Q^2, P^2)$. This leads to some underestimation of F_2^γ and the amount of this underestimation depends on the kinematics and geometry of each experiment. Some analyses have included P^2-dependent corrections in the systematic uncertainty (e.g. [15]). This problem is eliminated in the case of the electron structure function. Formula (9) enables any existing parametrisation of the photon structure function, both real ($P^2 = 0$) and virtual (P^2-dependent), to be tested against the measured electron structure function.

In this paper we report on the measurement of the electron structure function F_2^e using LEPI and LEPII data. Section 2 describes the selection process of the event sample collected for the analysis and the determination of the detector efficiency. Section 3 presents the measurement of the electron structure function F_2^e. Conclusions are given in Section 4.

2. Experimental procedure

2.1. The DELPHI detector

A detailed description of the DELPHI detector can be found in [16,17] and therefore only a short review of the sub-detectors relevant to the present analysis is given here. The DELPHI detector provided information on track curvature and 3-dimensional energy deposition with very good spatial resolution as well as identification of leptons and hadrons over most of the solid angle.

The most relevant parts of the setup for the electron structure function F_2^e analysis are divided into two groups. The first one consists of the detectors which were used in the reconstruction of the hadronic final state. They were: the Vertex Detector, the Inner Detector, the Time Projection Chamber (the main DELPHI tracking device) and the Outer Detector. Those devices were operated in a 1.23 T magnetic field parallel to the beam axis. Tracking in the forward (backward) regions was provided by the Forward Chambers. The tracking detectors covered polar angles from 20° to 160° at radii from 120 mm to 2060 mm for the barrel region. The Forward Chambers covered polar angles from 11° to 35° (forward sector) and 145°–169° (backward sector). Using these subsystems it was possible to reconstruct the charged particle momentum with a resolution $\frac{\sigma(p)}{p} \approx 0.0015 \cdot p$, where p is the momentum in GeV. The Hadron Calorimeter provided energy measurements of neutral particles.

The second group consists of detectors providing the electromagnetic shower energy measurement. The crucial one is the luminosity calorimeter STIC. The STIC was a lead-scintillator calorimeter formed by two cylindrical detectors placed on both sides of the DELPHI interaction point at a distance of 2200 mm and covered the angular region between 1.7° and 10.8° in polar angle at radii from 65 mm to 420 mm. The STIC energy measurements were used to define the tag condition.

2.2. Event selection

The analysis was carried out with the data samples collected by DELPHI at both LEPI and LEPII centre-of-mass energies ranging from 91.2 GeV up to 209.5 GeV and corresponding to integrated luminosities of 72 pb^{-1} at LEPI and 487 pb^{-1} at LEPII. A summary of the integrated luminosities used (along with the number of events selected for each sub-sample) is given in Table 1.

The most important criterion to select $\gamma\gamma$ events was that one of the two scattered electrons[3] was found in the STIC (tag-condition) whereas the second electron remained undetected (anti-tag condition). Such events were referred to as single-tag events. It

---

[3] Electron is used for both electron and positron.

Table 1

Nominal centre-of-mass energies, integrated luminosities of the data samples used and the corresponding numbers of selected events.

Experiment	Year	$\sqrt{s}$ (GeV)	Integrated L (pb^{-1})	Number of sel. events
LEPI	1994–1995	91	72	1507
LEPII	1996	172	10	198
	1997	183	53	1001
	1998	189	155	3398
	1999	196	76	1715
		200	83	1865
		202	40	901
	2000	205	70	1842

was required that the energy deposited by the tagged electron in the STIC was greater than $0.65 \cdot E$ and no additional energy clusters exceeding $0.25 \cdot E$ were detected in the STIC. The measured energy and angle of the scattered electron allow the virtuality, Q^2, of the probing photon to be determined. Due to the available phase space and correlations among selection cuts, as well as the requirement of good quality data, the range of Q^2 covered was narrower than that obtained from the angular limits of the DELPHI detector. An additional quality cut (minimal number of towers in STIC that fired) resulted in the effective polar angle θ_{tag} of the tagged electron being between $2.4°$ and $10°$.

The next step was to select $\gamma\gamma$ induced hadronic final states with a detected charged particle multiplicity greater than 3. Charged particles were defined as reconstructed tracks with momentum above 0.2 GeV, extrapolating to within 4 cm of the primary vertex in the transverse ($R\phi$) plane and within 10 cm along the beam direction (z-axis). The relative uncertainty in the momentum of a charged particle candidate, $\frac{\Delta p}{p}$, had to be smaller than 1, its polar angle with respect to the beam axis had to be between $20°$ and $160°$ and its measured track length in the TPC (Time Projection Chamber) greater than 40 cm. To satisfy the trigger condition at least one of the charged particles had to have a momentum greater than 0.7 GeV for LEPI data (1.0 GeV for LEPII data). The total energy of all charged particles had to be greater than 3 GeV and the minimum of the visible invariant mass[4] of all tracks, $W_{\gamma\gamma}$, was fixed at 3 GeV.

The Monte Carlo simulations of e^+e^- annihilation processes with PYTHIA [18–20] and four-fermion processes with EXCALIBUR [21] showed that the dominant background contributions came from Z^0 hadronic decays and the two-photon production of $\tau\tau$ pairs. In order to minimise these backgrounds, the following cuts were imposed:

- the vector sum of the transverse momenta of all charged particles, normalised to the total beam energy, $2E$, had to be greater than 0.12 for LEPI data (0.14 for LEPII data);
- the normalised (as above) sum of the absolute values of the longitudinal momenta of all charged particles (including the tagged electron) had to be greater than 0.6;
- the angle between the transverse momenta of the tagged electron and of the charged particle system had to be greater than $120°$;
- the maximum of the visible invariant mass was fixed at 40 GeV for LEPI data (60 GeV for LEPII data);
- the value of Q^2 had to be greater than 4 GeV^2 for LEPI (16 GeV^2 for LEPII).

Among the 21 430 events of the LEPI data set (101 913 for LEPII) with one high-energy deposit in the STIC calorimeter, 1507 events (10 920 for LEPII) passed the above criteria. The total background

[4] The invariant mass of all accepted charged particles.

contribution estimated from the simulation amounted to 111 events for LEPI (1027 for LEPII).

2.3. Efficiency analysis

In order to evaluate F_2^e one needs to measure two independent variables, the polar angle θ_{tag} of the scattered (tagged) electron and its energy, E_{tag}. The relative energy resolution was measured and parametrised as follows: $\frac{\sigma_E}{E} = 1.52 \oplus \frac{13.5}{\sqrt{E \text{ (GeV)}}}$ %, and the shower axis reconstruction precision was estimated to be in the range 9–15 mrad, depending on the particle energy. The measurement of these quantities allowed a direct determination of the z and Q^2 variables describing the electron structure function (see formulae (4), (5)).

The measured cross-sections were corrected for the detector inefficiency computed from a MC-generated sample of events passed through the detector simulation program and the selection criteria. As the efficiency computation was model dependent, it was very important to use an event-generator that described well the data events. In this analysis the TWOGAM [22] event generator coupled with the JETSET [19] Parton Shower algorithm for the quark and gluon fragmentation was used. The TWOGAM cross-sections consist of three independent components:

- the soft-hadronic part described by the Generalised Vector Dominance Model;
- the point-like component, QPM;
- the resolved photon interaction, RPC.

The GRV-LO [23] parametrisation of the photon structure function was adopted. More details can be found in [22]. To estimate the uncertainty coming from the model we have also used a sample of PYTHIA events. The selection criteria presented in Section 2.2 imposed on data (with integrated luminosity 72 pb^{-1} and 487 pb^{-1} for LEPI and LEPII respectively) have also been applied to both simulated samples (with an integrated luminosity 2500 pb^{-1} for each). The visible background-subtracted cross-sections for LEPII data as a function of: (1) cosine of the scattered electron angle $\cos(\theta_{tag})$, (2) the probing photon virtuality Q^2, (3) the scattered electron energy E_{tag}, and (4) the visible hadronic invariant mass $W_{\gamma\gamma}$ are compared to both simulated samples in Fig. 2. The TWOGAM distributions show better agreement with the real data cross-sections than those obtained with the PYTHIA event generator. All these discrepancies, both between real data and TWOGAM and real data and PYTHIA were taken into account in an estimate of the systematic uncertainties. Even though the visible cross-sections predicted by both generators were different, the efficiencies did not differ by more than about 5 percent, relative with respect to the TWOGAM model. In order to determine F_2^e the 2-dimensional efficiency functions, based on the TWOGAM model, were calculated for each chosen Q^2 range using $\Delta\xi_i \Delta Q_k^2$ bins, where $\xi_i = \log_{10}(z)$. The resulting efficiency varies between 10% and 70%.
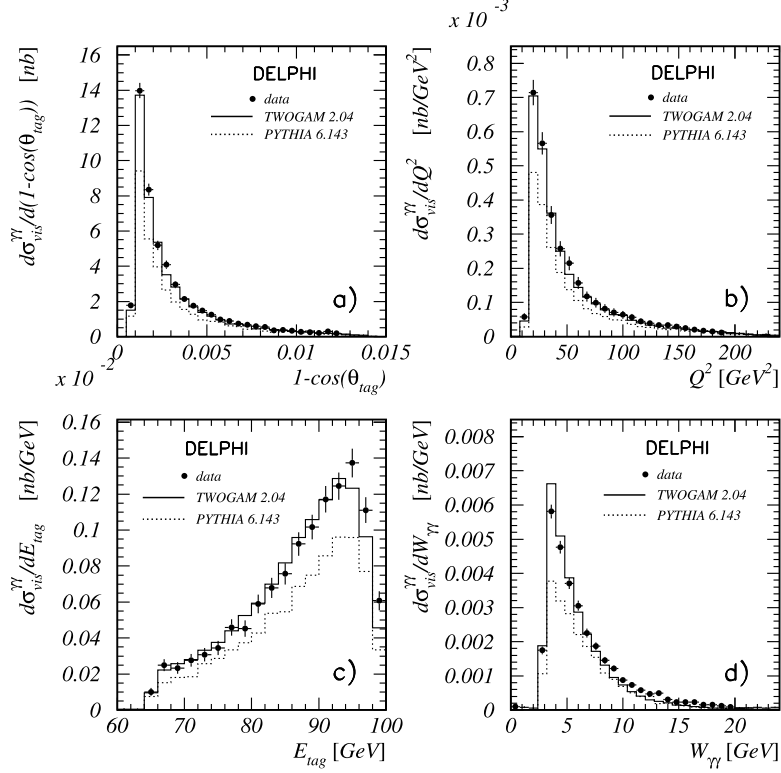
Fig. 2. Differential visible cross-sections (at LEPII energies) as a function of (a) cosine of the scattered electron angle θ_{tag}, (b) probing photon virtuality Q^2, (c) energy of scattered electron E_{tag}, (d) visible hadronic invariant mass, for real data (points with error bars) and simulation (histograms). Visible cross sections are defined as $\sigma_X = \frac{1}{L}\frac{\Delta N_{sel}}{\Delta X}$ where L is the integrated luminosity, N_{sel} is the number of selected events and X is the variable of interest.
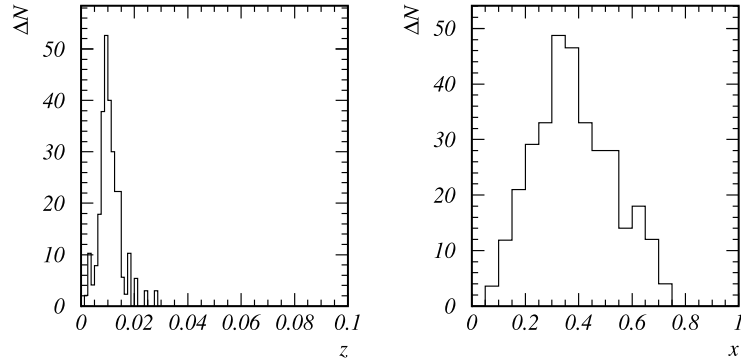

Fig. 3. The detector simulated z and x distributions obtained from event samples generated at $z = 0.01$ and $x = 0.1$ (LEPII) and for $Q^2 \in (20, 30)$ GeV^2. ΔN is the number of events per bin.

3. Determination of the electron structure function F_2^e

The electron structure function F_2^e can be extracted as a function of the two variables z and Q^2 from formula (2) under the assumption that the longitudinal term F_L^e contribution is negligible, which is justified in the kinematical range accessible at LEP energies [11],

$$F_2^e(\xi, Q^2) = \left(2\pi\alpha^2 \ln 10\right)^{-1}$$
$$\times \frac{Q^4}{(1 + (1-y)^2)} \frac{d^2\sigma(ee \rightarrow eeX)}{d\xi dQ^2}. \qquad (10)$$

The measured function $F_2^e(\xi, Q^2)^{meas}$ was corrected in each $\Delta\xi_i \Delta Q_k^2$ bin by the corresponding detector efficiency function $\epsilon(\xi, Q^2)$, yielding the reconstructed electron structure function

$F_2^e(\xi, Q^2)^{rec}$. Such a procedure is justified since the migration effect of events generated in any of the (ξ, Q^2) bins to neighbouring bins, after passing the detector simulation, was small. In Fig. 3 one can see the smearing caused by the detector for both, the standard photon x-variable Eq. (1) and the standard electron z-variable Eq. (4), for events with a fixed value of $x = 0.1$ and $z = 0.01$ generated and passed through the detector simulation program. Contrary to the narrow z distribution, the x distribution is shifted to higher values and spread over the whole region of x. For that reason the x distribution, related to the photon structure function, has to be treated in a special way by means of one or two-dimensional unfolding procedures. Both of them require theoretical knowledge of the kinematical distribution of the hadrons in the final state whereas the determination of the electron structure function F_2^e based on z is much less model-dependent.
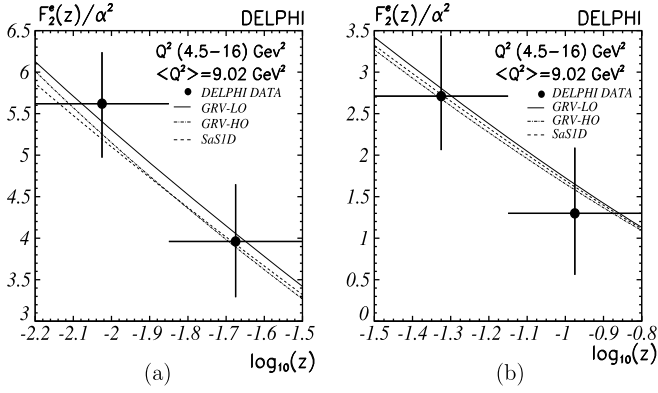
Fig. 4. LEPI data. The F_2^e measured for $Q^2 \in (4.5, 16)$ GeV^2. For better separation of the models presented the allowed interval of the ξ variable is split and shown separately in (a) and (b). For each bin the total uncertainty is plotted (the data are corrected for the absence of radiation in the theoretical prediction). Note, in Figs. 4 to 6 the data have been corrected to the bin centre, the horizontal bars are kept to indicate the range of the ξ (where $\xi = \log_{10}(z)$) variable.
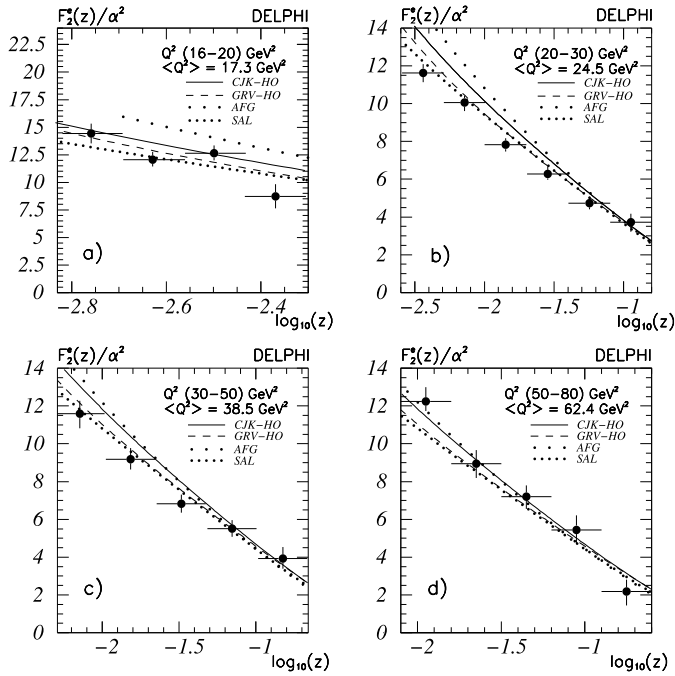

Fig. 5. LEPII data. F_2^e measured for (a) $Q^2 \in (16, 20)$ GeV^2, (b) $Q^2 \in (20, 30)$ GeV^2, (c) $Q^2 \in (30, 50)$ GeV^2, and (d) $Q^2 \in (50, 80)$ GeV^2. For each bin the total uncertainty is plotted (the data is corrected for the absence of radiation in the theoretical prediction). Note, that the AFG parametrisation is not available below $\log_{10}(z) = -2.7$.

The measured F_2^e was averaged over Q^2 in the region of the probing photon virtuality considered, leaving only the ξ dependence.[5] The electron structure function F_2^e is shown in Figs. 4–6 for six Q^2 intervals, $Q^2 \in (4.5, 16)$ GeV^2 for LEPI data as well as $Q^2 \in (16, 20)$ GeV^2, $Q^2 \in (20, 30)$ GeV^2, $Q^2 \in (30, 50)$ GeV^2, $Q^2 \in (50, 80)$ GeV^2 and $Q^2 \in (80, 200)$ GeV^2 for LEPII. Since the structure function obtained is integrated over the phase space of each bin, a correction to bin centre should be applied in order to convert it to a differential measurement at ξ_i. In order to estimate this correction the F_2^e at a given bin centre point ξ_i was calculated
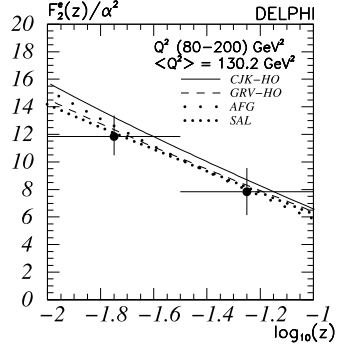

Fig. 6. LEPII data. The F_2^e measured for $Q^2 \in (80, 200)$ GeV^2. For each bin the total uncertainty is plotted (the data is corrected for the absence of radiation in the theoretical prediction).

(using theoretical predictions) and divided by the mean value of the F_2^e in this bin. The maximum correction coefficient obtained for the data analysed was approximately 4%.

Fig. 4 shows the electron structure function F_2^e extracted from LEPI data together with the GRV-LO (lowest-order), GRV-HO (higher-order) [24,23] and SaS1D [25] predictions for the photon structure function F_2^γ. In order to calculate F_2^e, F_2^γ was convoluted with the target photon flux factor according to Eqs. (8) and (9).

For LEPII data, Figs. 5–6, predictions for F_2^e based on recent NLO F_2^γ parameterisations, GRV-HO [24,23], AFG [26], CJK-HO [27], and SAL [28] are shown.

Due to the non-zero minimum polar tagging angle the untagged electron may still radiate a virtual photon up to $P^2 \approx 2$ GeV^2 at LEPI and $P^2 \approx 13$ GeV^2 at LEPII. As a consequence the effects of the target photon virtuality can be non-negligible. We have checked for the LEPII data at $Q^2 = 25$ GeV^2 that the inclusion of the P^2 dependence of F_2^γ changes the predictions by up to 10% [9]. One should stress that the virtualities of the target photons are by default included in the electron structure function whereas in the photon structure function analyses they are not.

Since radiative corrections (important for LEPII) were not incorporated into the theoretical predictions, the experimental data (Figs. 4–6) were corrected. The corrections were calculated using the TWOGAM generator that can produce both radiative-corrected and uncorrected data. Two large samples (corresponding to 2500 pb^{-1}) were generated and processed by the full detector simulation framework and the correction factors extracted. It was shown that the maximum value of the radiative correction was about 1.5% and 7% for LEPI and LEPII respectively.

For LEPI the data points follow the predictions of the earlier GRV-HO, GRV-LO and SaS1D models. For LEPII energies in the middle range of $Q^2 \in (20, 50)$ GeV^2 and for smaller values of ξ there is a general tendency for all parameterisations to lie slightly above the data points. This effect is clearer for the AFG and CJK-HO parameterisations. The measurements of the electron structure function F_2^e for LEPI and LEPII together with their statistical and systematic uncertainties are presented in Tables 2 and 3. The tables also contain the efficiencies $\epsilon(\xi)$ (averaged over the respective Q^2 range) and purities for each bin. The statistical uncertainties in each bin of the event distributions have been calculated according to the Poisson law and then propagated to the final distributions. The systematic uncertainty has the following contributions:

- the uncertainties due to the STIC detector calibration (corresponding to the absolute calibration error) of the electron energy ($\pm 0.13\%$) and scattering angle (± 0.45 mrad) of the tagged electron measurements. To estimate this contribution

---

[5] The phase space dependence of Q^2 versus the ξ and E variables translates into unequal intervals of ξ in Figs. 4–6.

Table 2
Results of the measurements of F_2^e for LEPI energies.

Q^2 (GeV²)	$\langle Q^2 \rangle$ (GeV²)	$-\xi$	$F_2^e(\xi)/\alpha^2$	σ_{stat}	σ_{syst}	σ_{total}	$\epsilon(\xi)$	Purity
(4.5–16)	9.02	0.80–1.15	1.30	±0.29	$^{+0.74}_{-0.69}$	$^{+0.79}_{-0.74}$	0.69	0.93
		1.15–1.50	2.71	±0.36	$^{+0.64}_{-0.54}$	$^{+0.73}_{-0.65}$	0.61	0.92
		1.50–1.85	3.96	±0.41	$^{+0.56}_{-0.53}$	$^{+0.69}_{-0.67}$	0.52	0.88
		1.85–2.20	5.62	±0.44	$^{+0.44}_{-0.48}$	$^{+0.62}_{-0.65}$	0.54	0.81

Table 3
Results of the measurements of F_2^e for LEPII energies.

Q^2 (GeV²)	$\langle Q^2 \rangle$ (GeV²)	$-\xi$	$F_2^e(\xi)/\alpha^2$	σ_{stat}	σ_{syst}	σ_{total}	$\epsilon(\xi)$	Purity
(16–20)	17.3	2.30–2.43	8.73	±0.92	$^{+0.47}_{-0.42}$	$^{+1.03}_{-1.01}$	0.53	0.89
		2.43–2.56	12.64	±0.50	$^{+0.47}_{-0.34}$	$^{+0.68}_{-0.61}$	0.50	0.90
		2.56–2.69	12.05	±0.49	$^{+0.46}_{-0.30}$	$^{+0.67}_{-0.57}$	0.52	0.84
		2.69–2.82	14.43	±0.54	$^{+0.61}_{-0.66}$	$^{+0.82}_{-0.85}$	0.60	0.83
(20–30)	24.5	0.80–1.10	3.71	±0.31	$^{+0.31}_{-0.40}$	$^{+0.44}_{-0.51}$	0.46	0.90
		1.10–1.40	4.73	±0.20	$^{+0.25}_{-0.22}$	$^{+0.32}_{-0.30}$	0.56	0.89
		1.40–1.70	6.27	±0.21	$^{+0.33}_{-0.22}$	$^{+0.39}_{-0.30}$	0.40	0.90
		1.70–2.00	7.82	±0.26	$^{+0.19}_{-0.23}$	$^{+0.32}_{-0.34}$	0.21	0.89
		2.00–2.30	10.06	±0.30	$^{+0.13}_{-0.29}$	$^{+0.33}_{-0.42}$	0.11	0.93
		2.30–2.60	11.63	±0.37	$^{+0.20}_{-0.26}$	$^{+0.42}_{-0.45}$	0.12	0.96
(30–50)	38.5	0.66–0.98	3.93	±0.40	$^{+0.41}_{-0.33}$	$^{+0.57}_{-0.51}$	0.56	0.91
		0.98–1.30	5.51	±0.35	$^{+0.31}_{-0.25}$	$^{+0.47}_{-0.43}$	0.57	0.90
		1.30–1.62	6.82	±0.40	$^{+0.24}_{-0.23}$	$^{+0.47}_{-0.46}$	0.36	0.86
		1.62–1.94	9.18	±0.48	$^{+0.32}_{-0.19}$	$^{+0.58}_{-0.52}$	0.18	0.93
		1.94–2.26	11.58	±0.61	$^{+0.24}_{-0.41}$	$^{+0.66}_{-0.73}$	0.11	0.95
(50–80)	62.4	0.60–0.90	2.18	±0.50	$^{+0.33}_{-0.54}$	$^{+0.60}_{-0.74}$	0.64	0.88
		0.90–1.20	5.44	±0.47	$^{+0.60}_{-0.49}$	$^{+0.76}_{-0.68}$	0.62	0.91
		1.20–1.50	7.20	±0.45	$^{+0.36}_{-0.43}$	$^{+0.58}_{-0.62}$	0.48	0.91
		1.50–1.80	8.95	±0.44	$^{+0.54}_{-0.51}$	$^{+0.69}_{-0.67}$	0.22	0.93
		1.80–2.10	12.24	±0.38	$^{+0.64}_{-0.33}$	$^{+0.74}_{-0.50}$	0.18	0.92
(80–200)	130.2	1.–1.5	7.84	±0.71	$^{+1.53}_{-1.56}$	$^{+1.69}_{-1.71}$	0.69	0.92
		1.5–2.0	11.84	±0.63	$^{+1.19}_{-1.37}$	$^{+1.35}_{-1.51}$	0.56	0.93

the energy E_{tag} and angle θ_{tag} of each tagged electron were varied by the calibration uncertainties successively. The structure function F_2^e was recomputed each time and the systematic uncertainty was taken as the maximum deviation between F_2^e values;

- the uncertainty due to binning variation. This was estimated by evaluating the structure function F_2^e for three different sets of binnings;
- the efficiencies resulting from the TWOGAM and PYTHIA models do not differ by more than about 5 percent and these differences were incorporated into the systematic uncertainties.

The systematic uncertainties were taken as fully correlated year-to-year.

Although the mass of the hadronic final state was not used explicitly in the analysis we applied a cut on the minimum invariant mass of hadronic particles (required by the Monte Carlo generators); a dedicated study showed that varying this cut had only a small impact on the F_2^e (below 1 percent effect) and it was decided not to include it in the systematic uncertainty. Also, the systematic uncertainties due to variations of the selection cuts (listed in Section 2.2) were negligible and have not been included.

4. Conclusions

The hadronic part of the electron structure function F_2^e has been measured and compared to various predictions of the photon structure function. The non-zero virtuality of the target photon can be taken into account in the photon flux as well as in the model of the photon structure function. It has been found that F_2^e agrees with the GRV-HO, SaS1D and SAL models. For lower values of the probing photon virtuality a discrepancy exists between the data and the predictions of the AFG and CJK-HO models. The presented analysis, based on directly measured quantities, is simpler than the photon structure function analysis because of the better resolution in the scaling variable. The statistical uncertainties in F_2^e are well understood since in each bin of z they directly reflect a Poisson error. In the photon analysis, because of the poor resolution in x, the unfolding procedure introduces a larger model-dependence of the statistical uncertainties. However, since a given value of z can be produced by a range of x values, the F_2^e may lose some of the discriminating power between models of the F_2^γ.

References

[1] E. Witten, Nucl. Phys. B 120 (1977) 189.
[2] C.H. Llewellyn Smith, Phys. Lett. B 79 (1978) 83.
[3] R.J. DeWitt, et al., Phys. Rev. D 19 (1979) 2046;
R.J. DeWitt, et al., Phys. Rev. D 20 (1979) 1751 (Erratum).
[4] T.F. Walsh, P. Zerwas, Phys. Lett. B 44 (1973) 195.
[5] R.L. Kingsley, Nucl. Phys. B 60 (1973) 45.
[6] W. Słomiński, J. Szwed, Phys. Lett. B 387 (1996) 861.
[7] W. Słomiński, J. Szwed, Acta Phys. Pol. B 27 (1996) 1887.
[8] W. Słomiński, J. Szwed, Acta Phys. Pol. B 28 (1997) 1493.
[9] W. Słomiński, J. Szwed, Eur. Phys. J. C 22 (2001) 123.
[10] W. Słomiński, Acta Phys. Pol. B 30 (1999) 369.
[11] R. Nisius, Phys. Rep. 332 (2000) 165.
[12] M. Krawczyk, A. Zembrzuski, M. Staszel, Phys. Rep. 345 (2001) 265.
[13] V.M. Budnev, I.F. Ginzburg, G.V. Meledin, V.G. Serbo, Phys. Rep. 15 (1975) 181.
[14] T. Uematsu, T.F. Walsh, Phys. Lett. B 101 (1981) 263.
[15] A. Heister, et al., ALEPH Collaboration, Eur. Phys. J. C 30 (2003) 145.
[16] P. Aarnio, et al., DELPHI Collaboration, Nucl. Instrum. Methods Phys. Res., Sect. A, Accel. Spectrom. Detect. Assoc. Equip. 303 (1991) 233.
[17] P. Abreu, et al., DELPHI Collaboration, Nucl. Instrum. Methods Phys. Res., Sect. A, Accel. Spectrom. Detect. Assoc. Equip. 378 (1996) 57.
[18] T. Sjöstrand, Comput. Phys. Commun. 82 (1994) 74.
[19] T. Sjöstrand, L. Lönnblad, S. Mrenna, P. Skands, PYTHIA 6.3 physics and manual, LU TP 03-38, arXiv:hep-ph/0308153.
[20] P. Aurenche, et al., in: Gamma–gamma Physics, 'Physics at LEP2', CERN 96-01 vol. 2, Sec. 5.5, 1996, p. 103.
[21] F.A. Berends, R. Pittau, R. Kleiss, Comput. Phys. Commun. 85 (1995) 437.
[22] T. Alderweireld, et al., in: S. Jadach, G. Passarino, R. Pittau (Eds.), Reports of the Working Groups on Precision Calculations for LEP2 Physics, CERN 2000-009, 2000, p. 219.
[23] M. Glück, E. Reya, A. Vogt, Phys. Rev. D 46 (1992) 1973.
[24] M. Glück, E. Reya, A. Vogt, Phys. Rev. D 45 (1992) 3986.
[25] G.A. Schuler, T. Sjöstrand, Phys. Lett. B 376 (1996) 193.
[26] P. Aurenche, M. Fontannaz, J.Ph. Guillet, Eur. Phys. J. C 44 (2005) 395.
[27] F. Cornet, P. Jankowski, M. Krawczyk, Phys. Rev. D 70 (2004) 093004.
[28] W. Slominski, H. Abramowicz, A. Levy, Eur. Phys. J. C 45 (2006) 633.